Ab initio calculations of the isotopic dependence of nuclear clustering

Serdar Elhatisari,[1,2] Evgeny Epelbaum,[3,4] Hermann Krebs,[3,4] Timo A. Lähde,[5]
Dean Lee,[6,4] Ning Li*,[5] Bing-nan Lu†,[5] Ulf-G. Meißner,[1,5,7] and Gautam Rupak[8]

[1]*Helmholtz-Institut für Strahlen- und Kernphysik and Bethe Center for Theoretical Physics, Universität Bonn, D-53115 Bonn, Germany*
[2]*Department of Physics, Karamanoglu Mehmetbey University, Karaman 70100, Turkey*
[3]*Institut für Theoretische Physik II, Ruhr-Universität Bochum, D-44870 Bochum, Germany*
[4]*Kavli Institute for Theoretical Physics, University of California, Santa Barbara, CA 93106-4030, USA*
[5]*Institute for Advanced Simulation, Institut für Kernphysik,*
and Jülich Center for Hadron Physics, Forschungszentrum Jülich, D-52425 Jülich, Germany
[6]*Department of Physics, North Carolina State University, Raleigh, NC 27695, USA*
[7]*JARA - High Performance Computing, Forschungszentrum Jülich, D-52425 Jülich, Germany*
[8]*Department of Physics and Astronomy and HPC^2 Center for Computational Sciences,*
Mississippi State University, Mississippi State, MS 39762, USA

Nuclear clustering describes the appearance of structures resembling smaller nuclei such as alpha particles (^{4}He nuclei) within the interior of a larger nucleus. While clustering is important for several well-known examples, little is known about the general nature of clustering in nuclei. In this letter we present lattice Monte Carlo calculations based on chiral effective field theory for the ground states of helium, beryllium, carbon, and oxygen isotopes. By computing model-independent measures that probe three- and four-nucleon correlations at short distances, we determine the effective number of alpha clusters in any nucleus as well as their shape compared to alpha particles in vacuum. We also introduce a new computational approach called the pinhole algorithm, which solves a long-standing deficiency of auxiliary-field Monte Carlo simulations in computing density correlations relative to the center of mass. We use the pinhole algorithm to determine the proton and neutron density distributions and the geometry of cluster correlations in ^{12}C, ^{14}C, and ^{16}C. The structural similarities among the carbon isotopes suggest that ^{14}C and ^{16}C have excitations analogous to the well-known Hoyle state resonance in ^{12}C [1, 2].

PACS numbers: 21.10.Dr, 21.30.-x, 21.60.De, 21.60.Gx

There have been many exciting recent advances in *ab initio* nuclear structure theory [3–10] which link nuclear forces to nuclear structure in impressive agreement with experimental data. However, we still know very little about the quantum correlations among nucleons that give rise to nuclear clustering and collective behavior. The main difficulty in studying alpha clusters in nuclei is that the calculation must include four-nucleon correlations. Unfortunately in many cases this dramatically increases the amount of computer memory and computing time needed in calculations of heavier nuclei. Nevertheless there is promising work in progress using the symmetry-adapted no-core shell model [11], antisymmetrized molecular dynamics [12], fermionic molecular dynamics [13], the alpha-container model [14], Monte Carlo shell model [15], and Green's function Monte Carlo [16].

Lattice calculations using chiral effective field theory and auxiliary-field Monte Carlo methods have probed alpha clustering in the ^{12}C and ^{16}O systems [17–20]. However these lattice simulations have encountered severe Monte Carlo sign oscillations in cases where the number of protons Z and number of neutrons N are different. In this work we solve this problem by using a new leading-order lattice action that retains a greater amount of symmetry, thereby removing nearly all of the Monte Carlo sign oscillations. The relevant symmetry is Wigner's SU(4) spin-isospin symmetry [21], where the four nucleon degrees of freedom can be rotated as four components of a complex vector. Previous attempts in taking this approach had failed due to the tendency of nuclei to overbind in larger nuclei. However recent progress has uncovered important connections between local interactions and nuclear binding as well as the significance of the alpha-alpha interaction [10, 22, 23]. Following this approach, we have constructed a leading-order lattice action with highly suppressed sign oscillations and which reproduces the ground-state binding energies of the hydrogen, helium, beryllium, carbon, and oxygen isotopes to an accuracy of 0.7 MeV per nucleon or better. We use auxiliary-field Monte Carlo simulations at leading order in chiral effective field theory with a spatial lattice spacing of 1.97 fm and lattice time spacing 1.97 fm$/c$. The lattice results are shown in Fig. 1 in comparison with the observed ground state energies. The full details of the lattice interaction, nucleon-nucleon phase shifts, simulation methods, and results are given in the Supplemental Materials.

Let $\rho(\mathbf{n})$ be the total nucleon density operator on lattice site $\mathbf{n}$. Similarly we define $\rho_p(\mathbf{n})$ as the proton density and $\rho_n(\mathbf{n})$ as the neutron density. We will use short-distance three- and four-nucleon operators as probes of the nuclear clusters. To construct a probe for alpha clusters, we define ρ_4 as the expectation value of $:\rho^4(\mathbf{n})/4!:$ summed over $\mathbf{n}$. The :: symbols indicate normal-ordering where all annihilation operators are moved to the right and all creation operators are moved to the left. For nuclei with even Z and even N, there are likely no well-defined ^{3}H or ^{3}He clusters since their formation is not energetically favorable. Therefore we can use short-distance three-nucleon operators as a second probe of alpha clusters. We define ρ_3 as the

FIG. 1: We show the ground state energies versus number of nucleons A for the hydrogen, helium, beryllium, carbon, and oxygen isotopes. The errors are one-standard deviation error bars associated with the stochastic errors and the extrapolation to an infinite number of time steps.

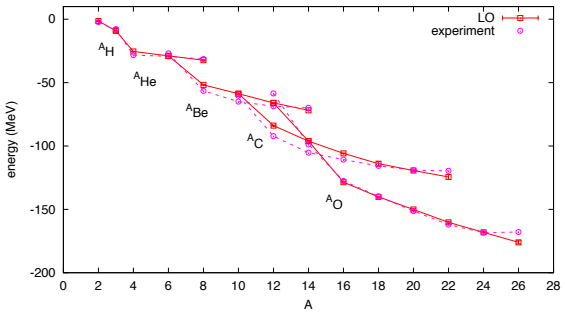

expectation value of : $\rho^3(\mathbf{n})/3!$: summed over $\mathbf{n}$. A ^{3}H or ^{3}He cluster may form in nuclei with odd Z or odd N. In this case we define ρ_{ppn} and ρ_{nnp} as the sum over $\mathbf{n}$ of the expectation values of : $\rho_p^2(\mathbf{n})\rho_n(\mathbf{n})/2$: and : $\rho_n^2(\mathbf{n})\rho_p(\mathbf{n})/2$: respectively. We use the difference $\rho_{ppn} - \rho_{nnp}$ as a probe of a possible ^{3}H or ^{3}He cluster. We can then define ρ_3 as the minimum of $2\rho_{ppn}$ and $2\rho_{nnp}$. The combinatorial factor of 2 is needed to match the previous definition for ρ_3 when ρ_{ppn} and ρ_{nnp} are equal. Since this quantity is unaffected by the three-nucleon cluster, it serves again as a second probe for alpha clusters. As we consider only nuclei with even Z and even N here, we focus on ρ_3 and ρ_4 for the remainder of the discussion.

Due to divergences at short distances, ρ_3 and ρ_4 will depend on the short-distance regularization scale, which in our case is the lattice spacing. However the regularization-scale dependence of ρ_3 and ρ_4 does not depend on the nucleus being considered. Therefore if we let $\rho_{3,\alpha}$ and $\rho_{4,\alpha}$ be the corresponding values for the alpha particle, then the ratios $\rho_3/\rho_{3,\alpha}$ and $\rho_4/\rho_{4,\alpha}$ are free from short-distance divergences and are model-independent quantities up to contributions from higher-dimensional operators in an operator product expansion. We have computed ρ_3 and ρ_4 for the helium, beryllium, and carbon isotopes. As our leading-order interactions are invariant under an isospin mirror flip that interchanges protons and neutrons, we focus here on neutron-rich nuclei. The results for ρ_3, ρ_4, $\rho_3/\rho_{3,\alpha}$ and $\rho_4/\rho_{4,\alpha}$ are presented in Table I. The values for ρ_3 and ρ_4 are given in dimensionless lattice units. As we might expect, the values for ρ_3 and ρ_4 are roughly the same for the different neutron-rich isotopes of each element.

Since ρ_4 involves four nucleons, it couples to the center of the alpha cluster while ρ_3 gets a contribution from a wider portion of the alpha-cluster wave function. Therefore, if we compute the ratio of $\rho_4/\rho_{4,\alpha}$ to $\rho_3/\rho_{3,\alpha}$, a value larger than one corresponds to more compact alpha clusters than in vacuum, and a value less than one corresponds to more diffuse alpha clusters. In Table I we observe that the ratio of $\rho_4/\rho_{4,\alpha}$ to $\rho_3/\rho_{3,\alpha}$ is very close to one when N is comparable to Z, but the ratio gradually decreases as the number of neutrons is increased. This indicates swelling of the alpha clusters as the system becomes saturated with excess neutrons.

We denote the number of alpha clusters as N_α. A simple counting of protons tells us that $N_\alpha = 1$ for neutron-rich helium, $N_\alpha = 2$ for neutron-rich beryllium, and $N_\alpha = 3$ for neutron-rich carbon. However the alpha clusters are immersed in a complex many-body system where nucleons of the same type are interchangeable. It is therefore useful to also define an "effective number" of alpha clusters that takes into account possible rearrangements of the nucleons into different alpha-cluster groupings. Since ρ_3 is less sensitive than ρ_4 to the detailed shape of the alpha clusters, we use $\rho_3/\rho_{3,\alpha}$ to give a rough estimate of the effective number of alpha clusters. If properly defined, the effective number of alpha clusters should be greater than or equal to N_α. A value equal to N_α indicates that the alpha clusters are behaving as indivisible objects, and the nucleus can be regarded as a compound fluid of alpha particles and neutrons. If the effective number is significantly greater than N_α, then the description in terms of individual alpha clusters breaks down and the system behaves more as a nuclear liquid of protons and neutrons. As the systems we consider are finite, this transition as a function of N and Z will be a smooth crossover.

We see in Table I that $\rho_3/\rho_{3,\alpha}$ is close to one for ^{6}He and ^{8}He. This is expected since the extra neutrons in these halo nuclei have relatively little binding energy. For the beryllium isotopes, the value of $\rho_3/\rho_{3,\alpha}$ is about 20% higher than the simple count $N_\alpha = 2$ for ^{8}Be, ^{10}Be, and ^{12}Be, and the excess rises to about 35% for ^{14}Be. For the carbon isotopes, the excess is about 25% for ^{12}C and rises to a maximum of about 50% excess near the drip line. So the description in terms of alpha particles and neutrons remains quite good for the beryllium isotopes and ^{12}C. For the neutron-rich carbon isotopes, the description in terms of alpha particles and neutrons degrades somewhat as more neutrons are added. We note that there is ample experimental evidence for the cluster properties of the neutron-rich beryllium and carbon isotopes [24–27].

Despite the many computational advantages of auxiliary-field Monte Carlo methods, one fundamental deficiency is that the simulations involve quantum states that are superpositions of many different center-of-mass positions. Therefore density distributions of the nucleons cannot be computed directly. To solve this problem we have developed a new method called the pinhole

TABLE I: We list ρ_3, ρ_4, $\rho_3/\rho_{3,\alpha}$ and $\rho_4/\rho_{4,\alpha}$ for the helium, beryllium, and carbon isotopes. The error bars denote one standard deviation errors associated with the stochastic errors and the extrapolation to an infinite number of time steps.

Nucleus	ρ_3	ρ_4	$\rho_3/\rho_{3,\alpha}$	$\rho_4/\rho_{4,\alpha}$
^{4}He	0.529(4)	0.0735(8)	1	1
^{6}He	0.546(5)	0.072(1)	1.03(1)	0.98(2)
^{8}He	0.510(6)	0.058(1)	0.96(1)	0.78(2)
^{8}Be	1.253(8)	0.181(2)	2.37(2)	2.46(4)
^{10}Be	1.25(2)	0.163(2)	2.36(4)	2.22(4)
^{12}Be	1.25(3)	0.15(1)	2.36(6)	2.0(1)
^{14}Be	1.414(7)	0.176(5)	2.67(2)	2.39(7)
^{12}C	2.03(2)	0.290(6)	3.83(5)	3.95(9)
^{14}C	2.21(4)	0.30(1)	4.17(9)	4.1(2)
^{16}C	2.31(3)	0.32(2)	4.37(6)	4.4(2)
^{18}C	2.25(1)	0.26(2)	4.24(4)	3.6(3)
^{20}C	2.39(2)	0.27(3)	4.51(5)	3.7(4)
^{22}C	2.27(2)	0.28(3)	4.29(9)	3.8(4)

algorithm. The pinhole algorithm behaves a bit like Maxwell's demon. An opaque screen is placed at the middle time step with pinholes bearing spin and isospin labels that allow nucleons with the corresponding spin and isospin to pass. We use A pinholes for a simulation of A nucleons, and the locations as well as the spin and isospin labels of the pinholes are updated by Monte Carlo importance sampling. From the simulations, we obtain the expectation value of the normal-ordered A-body density operator $: \rho_{i_1,j_1}(\mathbf{n}_1) \cdots \rho_{i_A,j_A}(\mathbf{n}_A) :$, where $\rho_{i,j}$ is the density operator for a nucleon with spin i and isospin j.

Using the pinhole algorithm, we have computed the proton and neutron densities for the ground states of ^{12}C, ^{14}C, and ^{16}C. In order to account for the nonzero size of the nucleons, we have convolved the point-nucleon distributions with a Gaussian distribution with root-mean-square radius 0.84 fm, the charge radius of the proton [28]. The results are shown in Fig. 2 along with the experimentally observed proton densities for ^{12}C and ^{14}C [29], which we define as the charge density divided by the electric charge e.

From Fig. 2 we see that the agreement between the calculated proton densities and experimental data for ^{12}C and ^{14}C is rather good. We show data for $L_t = 7, 9, 11, 13, 15$ time steps. The fact that the results have little dependence L_t means that we are seeing ground state properties. As we increase the number of neutrons and go from ^{12}C to ^{16}C, the shape of the proton density profile remains roughly the same. However there is a gradual decrease in the central density and a broadening of the proton density distribution. We see also that the excess neutrons in ^{14}C and ^{16}C are distributed fairly evenly, appearing in both the central region as well as the tail.

We now study the alpha-cluster structures of ^{12}C, ^{14}C, and ^{16}C in more detail. In order to probe the alpha cluster geometry, we use the fact that there is only one spin-up proton per alpha cluster. Using the pinhole algorithm, we consider the triangular shapes formed by the three spin-up protons in the carbon isotopes. This correlation function is free of short-distance divergences, and so, up to the contribution of higher-dimensional operators, it provides a model-independent measure that serves as a proxy for the geometry of the alpha-cluster configurations.

The three spin-up protons form the vertices of a triangle. When collecting the lattice simulation data, we rotate the triangle so that the longest side lies on the x-axis. We also rescale the triangle so the longest side has length one, and flip the triangle, if needed, so that the third spin-up proton is in the upper half of the xy-plane. Histograms of the third spin-up proton probability distributions for ^{12}C, ^{14}C, and ^{16}C are plotted in Fig. 3 using the data at $L_t = 15$ time steps. The data for other values of L_t are almost identical. There is some jaggedness due to the discreteness of the lattice, but we see quite clearly that the histograms for ^{12}C, ^{14}C, and ^{16}C are very similar. While there is some increase in the overall radius of the nucleus, the rescaled cluster geometry of the three carbon isotopes remain largely the same. In each case we see that there is a strong preference for triangles where the largest angle is less than or equal to 90 degrees.

Given the rich cluster structure of the excited states of ^{12}C, this raises the interesting possibility of similar cluster states appearing in ^{14}C and ^{16}C. In particular, the bound 0_2^+ state at 6.59 MeV above the ground state of ^{14}C may be a bound-state analog to the Hoyle state resonance in ^{12}C at 7.65 MeV. It may also have a clean experimental signature since low-lying neutron excitations are suppressed by the shell closure at eight neutrons. There is also a bound 0_2^+ in ^{16}C, however in this case one expects low-lying two-neutron excitations to be important, thereby making the analysis more complicated.

In order to analyze what we are seeing in the lattice data, we can make a simple Gaussian lattice model of the distribution of

FIG. 2: Plots of the proton and neutron densities for the ground states of ^{12}C, ^{14}C, and ^{16}C versus radial distance. We show data for $L_t = 7, 9, 11, 13, 15$ time steps. We show ^{12}C in panel **a**, ^{14}C in panel **b**, and ^{16}C in panel **c**. The errors are one-standard deviation error bars associated with the stochastic errors. For comparison we show the experimentally observed proton densities for ^{12}C and ^{14}C [29].

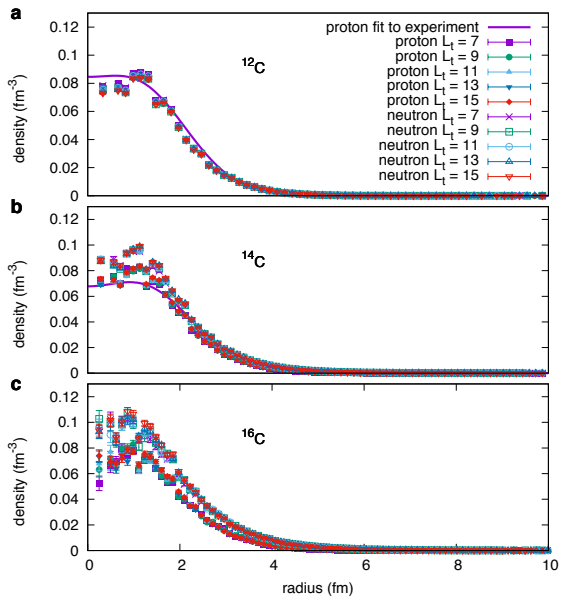

FIG. 3: The two red spheres with arrows indicate the first two spin-up protons, and the line connecting them is the longest side of the triangle. We show the third spin-up proton probability distribution in ^{12}C in panel **a**, ^{14}C in panel **b**, and ^{16}C in panel **c**. The results are computed at $L_t = 15$ time steps.

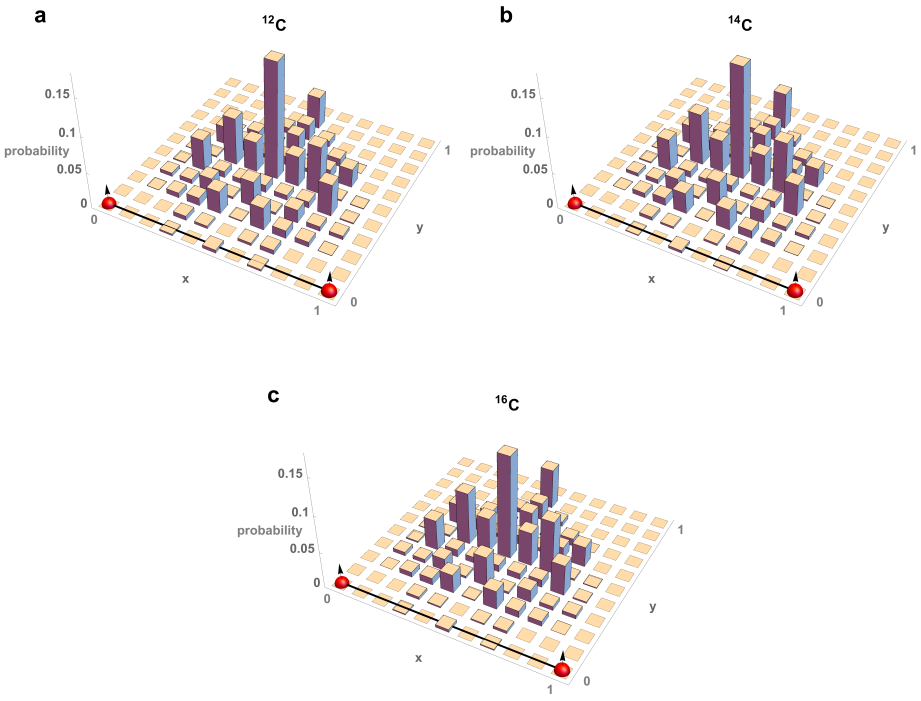

the spin-up protons. We consider a probability distribution $P(\vec{r}_1, \vec{r}_2, \vec{r}_3)$ on our lattice grid for the positions of the protons $\vec{r}_1$, $\vec{r}_2$, and $\vec{r}_3$. We take the probability distribution to be a product of Gaussians with root-mean-square radius 2.6 fm (charge radius

of ^{14}C) and unit step functions which vanish if the magnitude of $\vec{r}_1 - \vec{r}_2$, $\vec{r}_2 - \vec{r}_3$, or $\vec{r}_3 - \vec{r}_1$ is smaller than 1.7 fm (charge radius of ^{4}He). We can factor out the center-of-mass distribution of the three spin-up protons and recast the Gaussian factors as a product of Gaussians for the separation vectors $\vec{r}_1 - \vec{r}_2$, $\vec{r}_2 - \vec{r}_3$, and $\vec{r}_3 - \vec{r}_1$ with root-mean-square radius 4.5 fm. We show the third spin-up proton probability distribution corresponding to this model in Fig. 4. Despite the simplicity of this model with no free parameters, we note the good agreement with the lattice data for ^{12}C, ^{14}C, and ^{16}C. The only discrepancy is that the model overpredicts the probability of producing obtuse triangular configurations. This indicates that there are some additional correlations between the clusters that go beyond this simple Gaussian lattice model.

FIG. 4: The two red spheres with arrows indicate the first two spin-up protons, and the line connecting them is the longest side of the triangle. We show the third spin-up proton probability distribution using a simple Gaussian lattice model of the distribution of the spin-up protons.

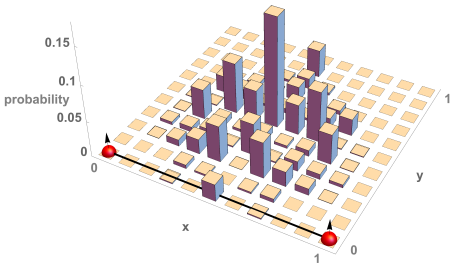

In this letter we have presented a number of novel approaches to computing and quantifying clustering in nuclei. We hope that this work may help to accelerate progress in theoretical and experimental efforts to understand the correlations that produce nuclear clustering and collective behavior.

Acknowledgement

We are grateful for the hospitality of the Kavli Institute for Theoretical Physics at UC Santa Barbara for hosting E.E, H.K., and D.L. We acknowledge partial financial support from the CRC110: Deutsche Forschungsgemeinschaft (SGB/TR 110, "Symmetries and the Emergence of Structure in QCD"), the BMBF (Verbundprojekt 05P2015 - NUSTAR R&D), the U.S. Department of Energy (DE-FG02-03ER41260), and U.S. National Science Foundation grant No. PHY-1307453. Further support was provided by the Magnus Ehrnrooth Foundation of the Finnish Society of Sciences and Letters and the Chinese Academy of Sciences (CAS) President's International Fellowship Initiative (PIFI) grant no. 2017VMA0025. The computational resources were provided by the Jülich Supercomputing Centre at Forschungszentrum Jülich, RWTH Aachen, and North Carolina State University.

Supplemental Materials

Lattice interactions

In our lattice simulations the spatial lattice spacing is taken to be $a = 1.97$ fm, and the time lattice spacing is $a_t = 1.97$ fm$/c$. The axial-vector coupling constant is $g_A = 1.29$, pion decay constant is $f_\pi = 92.2$ MeV, pion mass is $m_\pi = m_{\pi^0} = 134.98$ MeV, and nucleon mass is $m = 938.92$ MeV. We write σ_S with $S = 1, 2, 3$ for the spin Pauli matrices, and τ_I with $I = 1, 2, 3$ for the isospin Pauli matrices. We use dimensionless lattice units, where the physical quantities are multiplied by powers of the spatial lattice spacing a to make dimensionless combinations. We write α_t for the ratio a_t/a.

The notation $\sum_{\langle \mathbf{n}' \, \mathbf{n} \rangle}$ represents the summation over nearest-neighbor lattice sites of $\mathbf{n}$. We use $\sum_{\langle \mathbf{n}' \, \mathbf{n} \rangle_i}$ to indicate the sum over nearest-neighbor lattice sites of $\mathbf{n}$ along the $i^{\rm th}$ spatial axis. Similarly, $\sum_{\langle\langle \mathbf{n}' \, \mathbf{n} \rangle\rangle_i}$ is the sum over next-to-nearest-neighbor lattice sites of $\mathbf{n}$ along the $i^{\rm th}$ axis, and $\sum_{\langle\langle\langle \mathbf{n}' \, \mathbf{n} \rangle\rangle\rangle_i}$ is the sum over next-to-next-to-nearest-neighbor lattice sites of $\mathbf{n}$ along the $i^{\rm th}$ axis. Our lattice system is defined on an $L \times L \times L$ periodic cube, and so the summations over $\mathbf{n}'$ are defined with periodic boundary conditions.

In our notation $a_{\rm NL}$ is a four-component spin-isospin column vector while $a^\dagger_{\rm NL}$ is a four-component spin-isospin row vector. For real parameter $s_{\rm NL}$, we define the nonlocal annihilation and creation operators for each spin and isospin component of the nucleon,

$$a_{\rm NL}(\mathbf{n}) = a(\mathbf{n}) + s_{\rm NL} \sum_{\langle \mathbf{n}' \, \mathbf{n} \rangle} a(\mathbf{n}'), \tag{1}$$

$$a^\dagger_{\rm NL}(\mathbf{n}) = a^\dagger(\mathbf{n}) + s_{\rm NL} \sum_{\langle \mathbf{n}' \, \mathbf{n} \rangle} a^\dagger(\mathbf{n}'). \tag{2}$$

For spin indices $S = 1, 2, 3$, and isospin indices $I = 1, 2, 3$, we define point-like densities,

$$\rho(\mathbf{n}) = a^\dagger(\mathbf{n}) a(\mathbf{n}), \tag{3}$$

$$\rho_S(\mathbf{n}) = a^\dagger(\mathbf{n}) [\sigma_S] a(\mathbf{n}), \tag{4}$$

$$\rho_I(\mathbf{n}) = a^\dagger(\mathbf{n}) [\tau_I] a(\mathbf{n}), \tag{5}$$

$$\rho_{S,I}(\mathbf{n}) = a^\dagger(\mathbf{n}) [\sigma_S \otimes \tau_I] a(\mathbf{n}). \tag{6}$$

and also the smeared nonlocal densities,

$$\rho_{\rm NL}(\mathbf{n}) = a^\dagger_{\rm NL}(\mathbf{n}) a_{\rm NL}(\mathbf{n}), \tag{7}$$

$$\rho_{S,{\rm NL}}(\mathbf{n}) = a^\dagger_{\rm NL}(\mathbf{n}) [\sigma_S] a_{\rm NL}(\mathbf{n}), \tag{8}$$

$$\rho_{I,{\rm NL}}(\mathbf{n}) = a^\dagger_{\rm NL}(\mathbf{n}) [\tau_I] a_{\rm NL}(\mathbf{n}), \tag{9}$$

$$\rho_{S,I,{\rm NL}}(\mathbf{n}) = a^\dagger_{\rm NL}(\mathbf{n}) [\sigma_S \otimes \tau_I] a_{\rm NL}(\mathbf{n}). \tag{10}$$

For the leading-order short-range interactions we use

$$V_0 = \frac{c_0}{2} \sum_{\mathbf{n}', \mathbf{n}, \mathbf{n}''} : \rho_{\rm NL}(\mathbf{n}') f_{s_{\rm L}}(\mathbf{n}' - \mathbf{n}) f_{s_{\rm L}}(\mathbf{n} - \mathbf{n}'') \rho_{\rm NL}(\mathbf{n}'') : \tag{11}$$

where $f_{s_{\rm L}}$ is defined for real parameter s_L as

$$\begin{aligned} f_{s_{\rm L}}(\mathbf{n}) &= 1 \text{ for } |\mathbf{n}| = 0, \\ &= s_L \text{ for } |\mathbf{n}| = 1, \\ &= 0 \text{ otherwise.} \end{aligned} \tag{12}$$

The :: symbol indicates normal ordering, where the annihilation operators are on the right-hand side and the creation operators are on the left-hand side.

The one-pion exchange interaction is given by

$$V_{\rm OPE} = -\frac{g_A^2}{8 f_\pi^2} \sum_{\mathbf{n}', \mathbf{n}, S', S, I} : \rho_{S', I}(\mathbf{n}') f_{S' S}(\mathbf{n}' - \mathbf{n}) \rho_{S, I}(\mathbf{n}) :, \tag{13}$$

where $f_{S'S}$ is defined as

$$f_{S'S}(\mathbf{n}'-\mathbf{n}) = \frac{1}{L^3}\sum_{\mathbf{q}} \frac{\exp[-i\mathbf{q}\cdot(\mathbf{n}'-\mathbf{n}) - b_\pi \mathbf{q}^2] q_{S'} q_S}{\mathbf{q}^2 + m_\pi^2}, \tag{14}$$

and each q_S is an integer multiplied by $2\pi/L$. The parameter b_π removes short-distance lattice artifacts in the one-pion exchange interaction, and in this work we use the value $b_\pi = 0.700$. We take the free lattice Hamiltonian to have the form [30]

$$\begin{aligned} H_{\rm free} =& \frac{49}{12m}\sum_{\mathbf{n}} a^\dagger(\mathbf{n})a(\mathbf{n}) - \frac{3}{4m}\sum_{\mathbf{n},i}\sum_{\langle \mathbf{n}'\,\mathbf{n}\rangle_i} a^\dagger(\mathbf{n}')a(\mathbf{n}) \\ &+ \frac{3}{40m}\sum_{\mathbf{n},i}\sum_{\langle\langle \mathbf{n}'\,\mathbf{n}\rangle\rangle_i} a^\dagger(\mathbf{n}')a(\mathbf{n}) - \frac{1}{180m}\sum_{\mathbf{n},i}\sum_{\langle\langle\langle \mathbf{n}'\,\mathbf{n}\rangle\rangle\rangle_i} a^\dagger(\mathbf{n}')a(\mathbf{n}). \end{aligned} \tag{15}$$

The full leading-order (LO) lattice Hamiltonian can be written as

$$H_{\rm B} = H_{\rm free} + V_0 + V_{\rm OPE}, \tag{16}$$

with $s_{\rm NL} = 0.0800$, $s_{\rm L} = 0.0800$, and $c_0 = -0.1850$. In tuning our interactions here, we fit the parameters $s_{\rm NL}$, $s_{\rm L}$, and c_0 to the average inverse scattering length and effective range of the two s-wave channels, as well as the finite-volume energies of ^{8}Be. The finite-volume energies for ^{8}Be give a measure of the alpha-alpha scattering length, which was emphasized in Ref. [10] as a sensitive indicator correlated with the binding energies of medium-mass nuclei.

Nucleon-nucleon scattering

The details of the nucleon-nucleon scattering calculations are given in Ref. [10]. In Fig. S1 we show the LO lattice phase shifts for proton-neutron scattering versus the center-of-mass relative momentum. For comparison we also present phase shifts from the Nijmegen partial wave analysis [31]. In the first row, the data in panels **a**, **b**, **c**, **d** correspond to $^1s_0, ^3s_1, ^1p_1, ^3p_0$ respectively. In the second row, panels **e**, **f**, **g**, **h** correspond to $^3p_1, ^3p_2, ^1d_2, ^3d_1$ respectively. In the third row, panels **i**, **j**, **k**, **l** correspond to $^3d_2, ^3d_3, \varepsilon_1, \varepsilon_2$ respectively. These leading-order results are just the first step in the chiral effective field theory expansion, and the phase shifts would be systematically improved at each higher order, NLO, NNLO, etc.

Euclidean time projection and auxiliary-field Monte Carlo

The Euclidean time transfer matrix M is defined as the normal-ordered exponential of the lattice Hamiltonian H over one time lattice step,

$$M =: \exp[-H\alpha_t] : . \tag{17}$$

We use an initial state $|\Psi_i\rangle$ and final state $|\Psi_f\rangle$ that have nonzero overlap with the ground state nucleus of interest. By multiplying by powers of M upon $|\Psi_i\rangle$, we can project out the ground state. We compute projection amplitudes of the form

$$A_{fi}(L_t) = \langle \Psi_f | M^{L_t} | \Psi_i \rangle. \tag{18}$$

By calculating the ratio $A_{fi}(L_t)/A_{fi}(L_t-1)$ for large L_t we can determine the ground state energy.

It is useful to first prepare the initial state using a simpler transfer matrix M_* that is good approximation to M. We choose M_* to be invariant under Wigner's SU(4) symmetry [21]. The SU(4) symmetry eliminates sign oscillations from auxiliary-field Monte Carlo simulations of M_* [32, 33]. M_* has the same form as M, but the operator coefficients that violate SU(4) symmetry are turned off. We use M_* as an approximate low-energy filter by multiplying the initial and final states by M_* some fixed number of times, L_t',

$$A_{fi}(L_t) = \langle \Psi_f | M_*^{L_t'} M^{L_t} M_*^{L_t'} | \Psi_i \rangle. \tag{19}$$

We use auxiliary fields to generate the lattice interactions. The auxiliary field method can be viewed as a Gaussian integral formula which relates the exponential of the two-particle density, ρ^2, to the integral of the exponential of the one-particle density, ρ,

$$: \exp\left(-\frac{c\alpha_t}{2}\rho^2\right) : = \sqrt{\frac{1}{2\pi}}\int_{-\infty}^{\infty} ds : \exp\left(-\frac{1}{2}s^2 + \sqrt{-c\alpha_t}s\rho\right) : . \tag{20}$$

FIG. S1: We plot LO lattice phase shifts for proton-neutron scattering versus the center-of-mass relative momentum. For comparison we also plot the phase shifts extracted from the Nijmegen partial wave analysis [31]. In the first row, the data in panels **a**, **b**, **c**, **d** correspond to ${}^1s_0, {}^3s_1, {}^1p_1, {}^3p_0$ respectively. In the second row, panels **e**, **f**, **g**, **h** correspond to ${}^3p_1, {}^3p_2, {}^1d_2, {}^3d_1$ respectively. In the third row, panels **i**, **j**, **k**, **l** correspond to ${}^3d_2, {}^3d_3, \varepsilon_1, \varepsilon_2$ respectively.

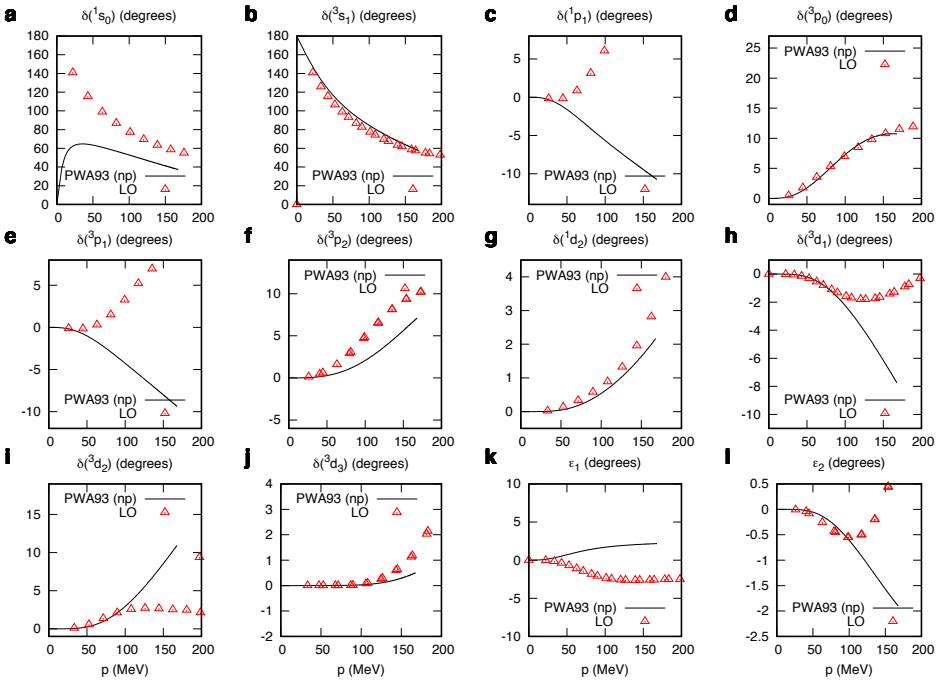

The normal ordering symbol :: ensures that the operator products of the creation and annihilation operators behave as classical anticommuting Grassmann variables [34]. We use this integral identity to introduce auxiliary fields at every lattice site [35–37]. The pion fields are treated in a manner similar to the auxiliary fields.

We couple the auxiliary field s to $\rho_{\rm NL}$ through a convolution with the smearing function $f_{s_{\rm L}}$. The linear term in the auxiliary field is

$$V_0^s = \sqrt{-c_0} \sum_{\mathbf{n},\mathbf{n}'} \rho_{\rm NL}(\mathbf{n}) f_{s_{\rm L}}(\mathbf{n}-\mathbf{n}') s(\mathbf{n}'), \tag{21}$$

and the quadratic term in the auxiliary field is

$$V_0^{ss} = \frac{1}{2} \sum_{\mathbf{n}} s^2(\mathbf{n}). \tag{22}$$

For the one-pion exchange interaction, the gradient of the pion field π_I is coupled to the point-like density $\rho_{S,I}$,

$$V^{\pi} = \frac{g_A}{2f_\pi} \sum_{\mathbf{n},\mathbf{n}',S,I} \rho_{S,I}(\mathbf{n}') f_S^{\pi}(\mathbf{n}'-\mathbf{n}) \pi_I(\mathbf{n}), \tag{23}$$

$$V^{\pi\pi} = \frac{1}{2} \sum_{\mathbf{n},\mathbf{n}',I} \pi_I(\mathbf{n}') f^{\pi\pi}(\mathbf{n}'-\mathbf{n}) \pi_I(\mathbf{n}) :, \tag{24}$$

where f_S^{π} and $f^{\pi\pi}$ are defined as

$$f_S^{\pi}(\mathbf{n}'-\mathbf{n}) = \frac{1}{L^3} \sum_{\mathbf{q}} \exp[-i\mathbf{q}\cdot(\mathbf{n}'-\mathbf{n})] q_S, \tag{25}$$

$$f^{\pi\pi}(\mathbf{n}'-\mathbf{n}) = \frac{1}{L^3} \sum_{\mathbf{q}} \exp[-i\mathbf{q}\cdot(\mathbf{n}'-\mathbf{n}) + b_\pi \mathbf{q}^2] (\mathbf{q}^2 + m_\pi^2). \tag{26}$$

Then the transfer matrix at leading order can be written as

$$: \exp\left(-H\alpha_t\right) := \int DsD\pi : \exp\left(-H_{\rm free}\alpha_t - V_0^s\sqrt{\alpha_t} - V_0^{ss} - V^\pi\alpha_t - V^{\pi\pi}\alpha_t\right) :, \tag{27}$$

where Ds is the path integral measure for s, and $D\pi$ is the path integral measure for π_I.

We use the same procedure for the initial states as discussed in Ref. [10], where four nucleons are inserted at each time step. For neutron-rich nuclei we also insert pairs of spin-up and spin-down neutrons, and for proton-rich nuclei we insert pairs of spin-up and spin-down protons. For the calculations of ^{3}H and ^{3}He we use an $L = 16\,\mathrm{fm}$ periodic box, and for the rest of the nuclei we use an $L = 12\,\mathrm{fm}$ periodic box.

Results for the ground state energies

In Fig. S2 we show the energy versus projection time for ^{3}H and ^{3}He. The error bars indicate one standard deviation errors due to the stochastic noise of the Monte Carlo simulations. The lines are extrapolations to infinite projection time using the functional form

$$E(t) = E_0 + c\exp[-\Delta E\, t], \tag{28}$$

where E_0 is the ground state energy that we wish to determine. The results for the helium isotopes are shown in Fig. S3, the beryllium isotopes in Fig. S4, the carbon isotopes in Fig. S5, and the oxygen isotopes in Fig. S6.

FIG. S2: We show the energy versus projection time for ^{3}H and ^{3}He. Since the leading-order action is isospin invariant, the results are the same for the two nuclei. The error bars indicate one standard deviation errors from the stochastic noise of the Monte Carlo simulations, and the line shows the extrapolation to infinite projection time.

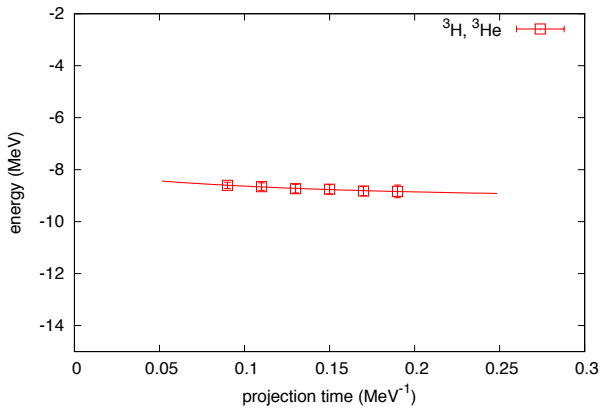

Results for ρ_3 and ρ_4

We compute ρ_3 by inserting the operator

$$: \exp\left[\sum_{\mathbf{n}} \epsilon(\mathbf{n})\rho(\mathbf{n})\right] : \tag{29}$$

at the middle time step and taking three numerical derivatives with respect to $\epsilon(\mathbf{n})$ for infinitesmally small $\epsilon(\mathbf{n})$. We then divide by 3! and sum over $\mathbf{n}$. For ρ_4 we compute four numerical derivatives with respect to $\epsilon(\mathbf{n})$, divide by 4!, and sum over $\mathbf{n}$.

In Fig. S7 we show ρ_3 versus projection time for the neutron-rich helium, beryllium, and carbon isotopes. The error bars indicate one standard deviation errors due to the stochastic noise of the Monte Carlo simulations. The lines are extrapolations to infinite projection time using the functional forms

$$\rho_3(t) = \rho_3 + c_3\exp[-\Delta E\, t/2], \tag{30}$$

$$\rho_4(t) = \rho_4 + c_4\exp[-\Delta E\, t/2], \tag{31}$$

FIG. S3: We show the energy versus projection time for the helium isotopes. The error bars indicate one standard deviation errors from the stochastic noise of the Monte Carlo simulations, and the lines show extrapolations to infinite projection time.

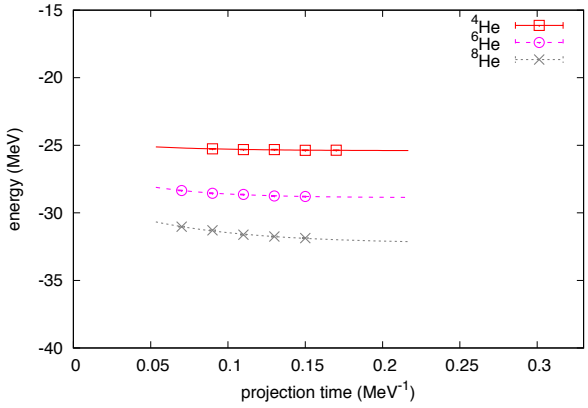

FIG. S4: We show the energy versus projection time for the beryllium isotopes. The error bars indicate one standard deviation errors from the stochastic noise of the Monte Carlo simulations, and the lines show extrapolations to infinite projection time.

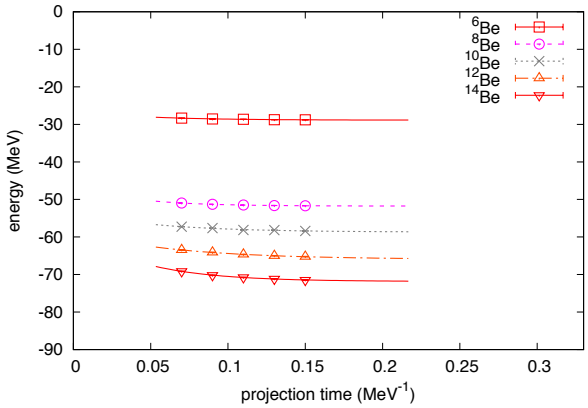

FIG. S5: We show the energy versus projection time for the carbon isotopes. The error bars indicate one standard deviation errors from the stochastic noise of the Monte Carlo simulations, and the lines show extrapolations to infinite projection time.

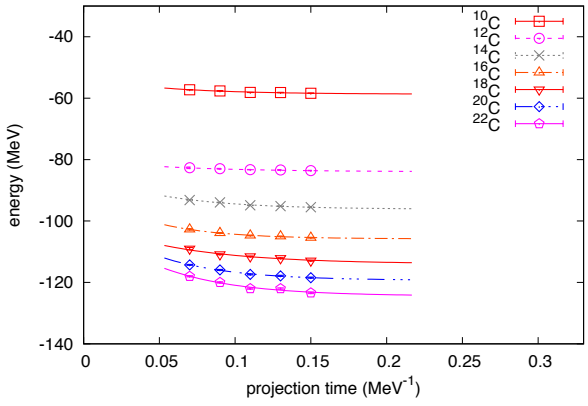

where ΔE is determined from the ground state energy fit in Eq. (28). The factor of $t/2$ rather than t reflects the fact that there are exponential corrections from matrix elements connecting the ground state to the first excited state. In Fig. S8 we show ρ_4 versus projection time for the neutron-rich helium, beryllium, and carbon isotopes.

FIG. S6: We show the energy versus projection time for the oxygen isotopes. The error bars indicate one standard deviation errors from the stochastic noise of the Monte Carlo simulations, and the lines show extrapolations to infinite projection time.

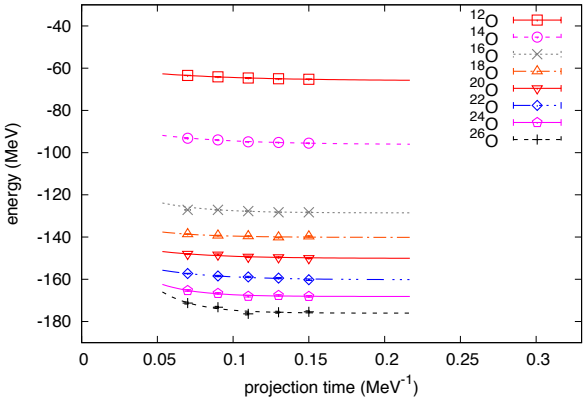

FIG. S7: We show ρ_3 versus projection time for the neutron-rich helium, beryllium, and carbon isotopes. The error bars indicate one standard deviation errors from the stochastic noise of the Monte Carlo simulations, and the lines show extrapolations to infinite projection time.

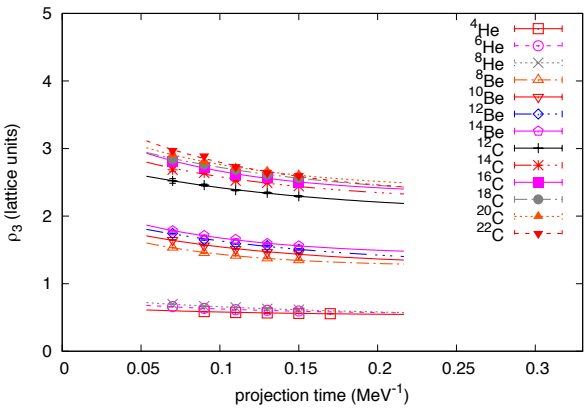

FIG. S8: We show ρ_4 versus projection time for the neutron-rich helium, beryllium, and carbon isotopes. The error bars indicate one standard deviation errors from the stochastic noise of the Monte Carlo simulations, and the lines show extrapolations to infinite projection time.

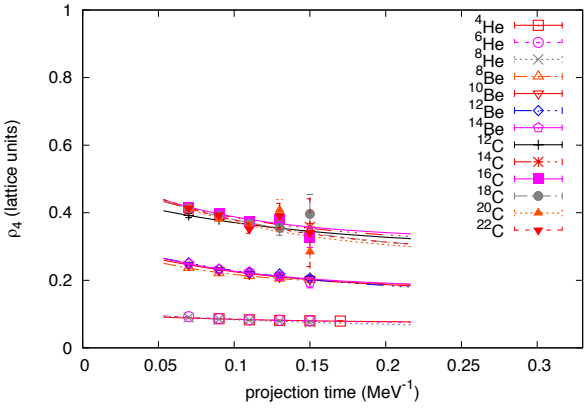

Pinhole algorithm and density correlations

Auxiliary-field Monte Carlo simulations are efficient for computing the quantum properties of systems with attractive pairing interactions. By the calculating the exact quantum amplitude for each configuration of auxiliary fields, we obtain the full set

of correlations induced by the interactions. However, the exact quantum amplitude for each auxiliary field configuration involves quantum states which are superpositions of many different center-of-mass positions. Therefore information about density correlations relative to the center of mass is lost. The pinhole algorithm is a new computational approach that allows for the calculation of arbitrary density correlations with respect to the center of mass. As this was not possible in all previous auxiliary-field Monte Carlo simulations, adaptations of this technique should have wide applications to hadronic, nuclear, condensed matter, and ultracold atomic simulations.

We let $\rho_{i,j}(\mathbf{n})$ be the density operator for nucleons with spin i and isospin j at lattice site $\mathbf{n}$,

$$\rho_{i,j}(\mathbf{n}) = a^\dagger_{i,j}(\mathbf{n}) a_{i,j}(\mathbf{n}). \tag{32}$$

We construct the normal-ordered A-body density operator

$$\rho_{i_1,j_1,\cdots i_A,j_A}(\mathbf{n}_1,\cdots \mathbf{n}_A) = :\rho_{i_1,j_1}(\mathbf{n}_1)\cdots\rho_{i_A,j_A}(\mathbf{n}_A):. \tag{33}$$

In the A-nucleon subspace, we note the completeness identity

$$\sum_{i_1,j_1,\cdots i_A,j_A}\sum_{\mathbf{n}_1,\cdots \mathbf{n}_A} \rho_{i_1,j_1,\cdots i_A,j_A}(\mathbf{n}_1,\cdots \mathbf{n}_A) \ = A!. \tag{34}$$

The new feature of the pinhole algorithm is that Monte Carlo importance sampling is performed according to the absolute value of the expectation value

$$\langle \Psi_f | M_*^{L_t'} M^{L_t/2} \rho_{i_1,j_1,\cdots i_A,j_A}(\mathbf{n}_1,\cdots \mathbf{n}_A) M^{L_t/2} M_*^{L_t'} | \Psi_i\rangle. \tag{35}$$

Due to the completeness identity Eq. (34), the sum of the amplitude in Eq. (35) over $\mathbf{n}_1,\cdots \mathbf{n}_A$ and $i_1,j_1,\cdots i_A,j_A$ gives $A!$ times the amplitude without any insertion of the A-body density,

$$\langle \Psi_f | M_*^{L_t'} M^{L_t} M_*^{L_t'} | \Psi_i\rangle. \tag{36}$$

The pinhole locations $\mathbf{n}_1,\cdots \mathbf{n}_A$ and spin-isospin indices $i_1,j_1,\cdots i_A,j_A$ are sampled by Metropolis updates [38], while the auxiliary fields are sampled by the hybrid Monte Carlo algorithm [39, 40]. In Fig. S9 we show a sketch of the pinhole locations and spin-isospin indices for the operator $\rho_{i_1,j_1,\cdots i_A,j_A}(\mathbf{n}_1,\cdots \mathbf{n}_A)$ inserted at time $t = L_t a_t/2$. We obtain the ground state expectation value by extrapolating to the limit of infinite projection time.

FIG. S9: A sketch of the pinhole locations and spin-isospin indices at time $t = L_t a_t/2$.

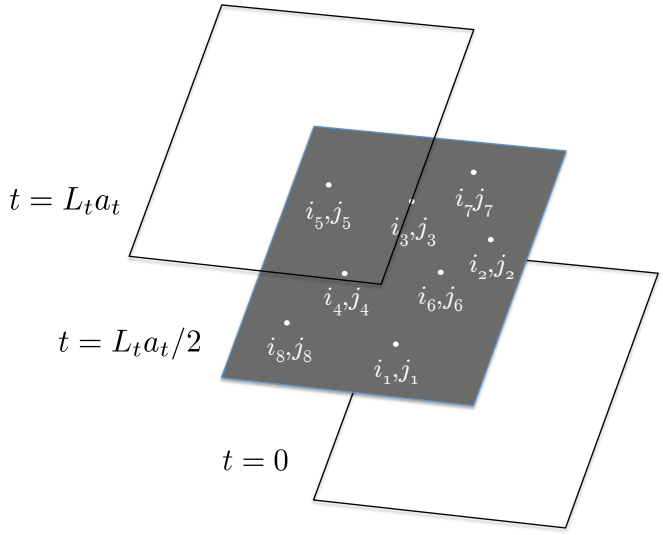

For spatial lattice spacing a, the coordinates $\mathbf{r}_i$ of each nucleon on the lattice is an integer vector $\mathbf{n}_i$ times a. We do not consider mass differences between protons and neutrons in these calculations. Since the center of mass is a mass-weighted average of A nucleons with the same mass, the center-of-mass position $\mathbf{r}_{\rm CM}$ is an integer vector $\mathbf{n}_{\rm CM}$ times a/A. Therefore the

density distribution has a resolution scale that is A times smaller than the lattice spacing. In order to determine the center-of-mass position $\mathbf{r}_{\rm CM}$, we minimize the squared radius

$$\sum_i |\mathbf{r}_{\rm CM} - \mathbf{r}_i|^2 \,, \tag{37}$$

where each term $|\mathbf{r}_{\rm CM} - \mathbf{r}_i|$ is minimized with respect to all periodic copies of the separation distance on the lattice. We comment that the tails of the proton and neutron density distributions are determined from the asymptotic properties of the A-body wave function, which have been derived in a recent paper [41] for interactions with finite range.

As discussed in the main text, from the A-body density information we can view the triangular shapes formed by the three spin-up protons in the carbon isotopes. The positions of the three spin-up protons serve as a measure of the alpha cluster geometry. In Fig. S10 we sketch a typical configuration of the protons (red) and neutrons (blue) with the arrows indicating up and down spins in ^{12}C. The three spin-up protons form the vertices of a triangle, and this is indicated by the orange triangle in Fig. S10. When collecting the lattice simulation data, we rotate the triangle so that the longest side lies on the x-axis. We also rescale the triangle so the longest side has length one, and flip the triangle, if needed, so that the third spin-up proton is in the upper half of the xy-plane.

FIG. S10: We sketch a typical configuration of the protons (red) and neutrons (blue) in ^{12}C, with the arrows indicating up and down spins. The triangle of spin-up protons is indicated by the orange triangle.

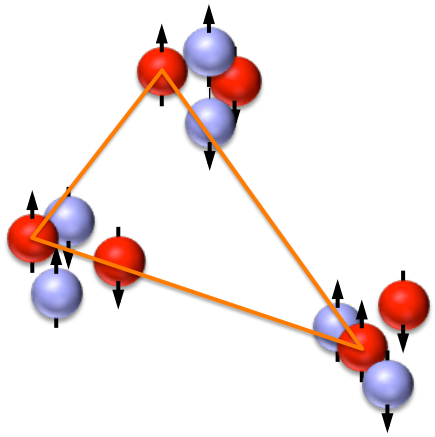

[1] F. Hoyle, Astrophys. J. Suppl. **1**, 121 (1954).
[2] C. Cook, W. A. Fowler, C. C. Lauritsen, and T. Lauritsen, Phys. Rev. **107**, 508 (1957).
[3] C. Romero-Redondo, S. Quaglioni, P. Navratil, and G. Hupin, Phys. Rev. Lett. **113**, 032503 (2014), 1404.1960.
[4] P. Maris, J. P. Vary, A. Calci, J. Langhammer, S. Binder, and R. Roth, Phys. Rev. **C90**, 014314 (2014), 1405.1331.
[5] T. Dytrych, P. Maris, K. D. Launey, J. P. Draayer, J. P. Vary, D. Langr, E. Saule, M. A. Caprio, U. Catalyurek, and M. Sosonkina, Comput. Phys. Commun. **207**, 202 (2016), 1602.02965.
[6] T. Duguet, V. Soma, S. Lecluse, C. Barbieri, and P. Navratil (2016), 1611.08570.
[7] S. R. Stroberg, A. Calci, H. Hergert, J. D. Holt, S. K. Bogner, R. Roth, and A. Schwenk, Phys. Rev. Lett. **118**, 032502 (2017), 1607.03229.
[8] R. F. Garcia Ruiz et al., Nature Phys. **12**, 594 (2016), 1602.07906.
[9] G. Hagen, G. R. Jansen, and T. Papenbrock, Phys. Rev. Lett. **117**, 172501 (2016), 1605.01477.
[10] S. Elhatisari et al., Phys. Rev. Lett. **117**, 132501 (2016), 1602.04539.
[11] K. D. Launey, T. Dytrych, and J. P. Draayer, Prog. Part. Nucl. Phys. **89**, 101 (2016), 1612.04298.
[12] Y. Yoshida and Y. Kanada-En'yo (2016), 1609.01407.
[13] H. Feldmeier and T. Neff (2016), 1612.02602.
[14] P. Schuck, Y. Funaki, H. Horiuchi, G. Roepke, A. Tohsaki, and T. Yamada, Phys. Scripta **91**, 123001 (2016), 1702.02191.
[15] T. Yoshida, N. Shimizu, T. Abe, and T. Otsuka, J. Phys. Conf. Ser. **569**, 012063 (2014).
[16] A. Lovato, S. Gandolfi, J. Carlson, S. C. Pieper, and R. Schiavilla, Phys. Rev. Lett. **117**, 082501 (2016), 1605.00248.
[17] E. Epelbaum, H. Krebs, D. Lee, and U.-G. Meißner, Phys. Rev. Lett. **106**, 192501 (2011), 1101.2547.
[18] E. Epelbaum, H. Krebs, T. Lähde, D. Lee, and U.-G. Meißner, Phys. Rev. Lett. **109**, 252501 (2012), 1208.1328.
[19] E. Epelbaum, H. Krebs, T. A. Lähde, D. Lee, and U.-G. Meißner, Phys. Rev. Lett. **110**, 112502 (2013), 1212.4181.
[20] E. Epelbaum, H. Krebs, T. A. Lähde, D. Lee, U.-G. Meißner, and G. Rupak, Phys. Rev. Lett. **112**, 102501 (2014), 1312.7703.
[21] E. Wigner, Phys. Rev. **51**, 106 (1937).
[22] S. Elhatisari, D. Lee, G. Rupak, E. Epelbaum, H. Krebs, T. A. Lähde, T. Luu, and U.-G. Meißner, Nature **528**, 111 (2015), 1506.03513.
[23] A. Rokash, E. Epelbaum, H. Krebs, and D. Lee (2016), 1612.08004.
[24] H. G. Bohlen, T. Dorsch, T. Kokalova, W. von Oertzen, C. Schulz, and C. Wheldon, Nucl. Phys. **A787**, 451 (2007).
[25] H. G. Bohlen et al., Nucl. Phys. **A722**, C3 (2003).
[26] M. Freer, AIP Conf. Proc. **1072**, 58 (2008).
[27] D. J. Marin-Lambarri, R. Bijker, M. Freer, M. Gai, T. Kokalova, D. J. Parker, and C. Wheldon, Phys. Rev. Lett. **113**, 012502 (2014), 1405.7445.
[28] R. Pohl et al., Nature **466**, 213 (2010).
[29] F. J. Kline, H. Crannell, J. T. O' Brien, J. Mccarthy, and R. R. Whitney, Nucl. Phys. **A209**, 381 (1973).
[30] E. Epelbaum, H. Krebs, D. Lee, and U.-G. Meißner, Eur. Phys. J. **A45**, 335 (2010), 1003.5697.
[31] V. G. J. Stoks, R. A. M. Kompl, M. C. M. Rentmeester, and J. J. de Swart, Phys. Rev. **C48**, 792 (1993).
[32] J.-W. Chen, D. Lee, and T. Schäfer, Phys. Rev. Lett. **93**, 242302 (2004), nucl-th/0408043.
[33] D. Lee, Phys. Rev. Lett. **98**, 182501 (2007), nucl-th/0701041.
[34] D. Lee, Prog. Part. Nucl. Phys. **63**, 117 (2009), 0804.3501.
[35] J. Hubbard, Phys. Rev. Lett. **3**, 77 (1959).
[36] R. L. Stratonovich, Soviet Phys. Doklady **2**, 416 (1958).
[37] S. E. Koonin, Journal of Statistical Physics **43**, 985 (1986), ISSN 0022-4715.
[38] W. K. Hastings, Biometrika **57**, 97 (1970).
[39] S. Duane, A. D. Kennedy, B. J. Pendleton, and D. Roweth, Phys. Lett. **B195**, 216 (1987).
[40] S. Gottlieb, W. Liu, D. Toussaint, R. L. Renken, and R. L. Sugar, Phys. Rev. **D35**, 2531 (1987).
[41] S. König and D. Lee (2017), 1701.00279.